COMMUNICATIONS CHEMISTRY

ARTICLE

https://doi.org/10.1038/s42004-019-0189-1 OPEN

Visualizing hydrogen diffusion in magnetic film through magneto-optical Kerr effect

Po-Chun Chang[1], Yun-Ying Chang[1], Wei-Hsiang Wang[1], Fang-Yuh Lo[1] & Wen-Chin Lin[1]

The kinematics of hydrogen diffusion in nontransparent metallic materials is crucial to the hydrogen-sensing and -storage technology and remains a challenge. Alongside the conventional optical investigations, the hydrogen absorption-induced reversible changes of magnetic properties in ferromagnetic thin films provides a new method for visualization of hydrogen in solids. Here we monitor real-time hydrogen diffusion in a cobalt-palladium alloy ($Co_{25}Pd_{75}$) film using a magneto-optical Kerr microscope. The spatially resolved magneto-optical contrasted images provide a noninvasive method of monitoring hydrogen movement. Hydrogen diffusion follows Fick's diffusion law, and a diffusion coefficient of $3 \pm 2 \times 10^{-12}$ m^2/s is obtained. The diffusion velocity of the 2–4% hydrogen concentration fronts reaches 30 ± 15 nm/s in the uniform film area and increases to 50 ± 20 nm/s near a defect site. These results can be applied in detecting hydrogen diffusion in other spintronic materials, such as magnetic palladium-alloy thin films.

[1] Department of Physics, National Taiwan Normal University, 11677 Taipei, Taiwan. Correspondence and requests for materials should be addressed to W.-C.L. (email: wclin@ntnu.edu.tw)

Because of limited fossil fuel resources and increasing energy demands, hydrogen will be a crucial element in future renewable energy[1]. Numerous studies have been undertaken to identify functional materials for sensing, storage, and catalyzed dissociation of hydrogen, yet these remain a challenge[1,2]. In addition to the conventional gas phase, hydrogen can be stored in the interstitial sites of a solid crystalline lattice after dissociation from bi-atomic molecules to single atoms[2]. Because the volumetric density of hydrogen can be greatly increased in solid state storage, various metal-hydride systems have been investigated for their hydrogen storage potential. Moreover, after hydrogen absorption, the crystalline structure, electronic properties, and magnetism of the materials usually change; therefore, materials sensitive to hydrogen absorption have been proposed for use in hydrogen-sensing devices. Most studies have focused on reversible optical and electrical property changes induced by hydrogenation[3,4]. Hydrogen-induced reduction of resistivity can feasibly be applied to hydrogen sensing, but it cannot provide spatial resolution of hydrogen content in the materials. Hydrogen-induced changes of optical properties, especially transmission, provide a noninvasive method of detecting hydrogen diffusion in materials. Huiberts et al.[3] first reported the switchable optical properties of yttrium and lanthanum hydride films[3]. Upon hydrogen loading, yttrium hydride changes from a shiny mirror to a transparent window. Den Broeder et al.[5] pioneered the visualization of hydrogen migration in solids using YH_x switchable mirror thin films. They observed the electromigration of hydrogen, which diffused toward the anode when a current flowed through the film. This indicated that hydrogen in $YH_{3-\delta}$ behaved as a negative ion. Kerssemakers et al.[6] observed the homogeneous and essentially independent optical switching of individual domains in $Pd/YH_x/CaF_2(111)$ epitaxial switchable mirrors during hydrogen absorption. Remhof et al.[7] demonstrated that YH_x switchable mirror material could be used both as an indicator for monitoring and an agent for controlling hydrogen diffusion in a VH_x underlayer. Hjörvarsson and colleagues[8] combined light and electron scattering to explore hydrogen diffusion in Pd/V/MgO(001) single crystalline thin metallic films.

Most studies have used reflectivity and transmission changes in YH_x and VH_x, respectively, to visualize hydrogen diffusion[3,5–8]. However, investigating the kinetics of hydrogen diffusion in other nontransparent metallic materials remains a challenge. Alongside the reported optical investigations, the reversible changes of magnetic properties in ferromagnetic thin films induced by hydrogen absorption and desorption should also be considered[9–13]. This method can be applied to various hydrogen-sensitive magnetic Pd-alloys, in which the detection of hydrogen-induced magnetism changes is feasible even though hydrogen-induced change in reflectivity is limited. Our other studies showed that in an annealed Pd/Co/Pd trilayer and a $[Co/Pd]_{12}$ multilayer, hydrogenation-induced modulation of magnetism could be observed because of the Pd-alloyed interface effect[13–17]. This was because Pd is a highly efficient catalyst for hydrogen molecule dissociation and Pd-hydride formation is energy favorable[2]. Based on these findings, we also observed appreciable magnetic modulation in Pd-rich magnetic alloy thin films, indicating that such materials would be useful in fabricating gas sensors and especially suitable for spatially resolved hydrogen diffusion[12,18–23]. Moreover magneto-optical Kerr effect (MOKE), originating from the optical property and magnetism of materials, has long been widely applied in magnetic measurement of nanoscale samples because of the extremely high sensitivity and feasibility[24–26]. In addition to the magneto-optical Kerr rotation and intensity, the intrinsic characteristics of magnetism such as the magnetic cercivity H_c and the squareness M_r/M_s can be measured through this method[14,16,18,23,27,28].

Here we demonstrate hydrogen diffusion monitoring in a $Co_{25}Pd_{75}/SiO_2/Si(100)$ magnetic film using a magneto-optical Kerr microscope in the longitudinal geometry. The spatial distribution of hydrogen content is recorded with variations in absorption and desorption time, respectively. The detailed kinetics of hydrogen diffusion are also discussed in this paper.

Results

Sample design and measurement of magneto-optical Kerr effect. Figure 1 illustrates a sample structure with the measurement geometry. The right side of a 50-nm-thick $Co_{25}Pd_{75}$ alloy stripe was fully covered by a 100-nm-thick ZnO film. ZnO is transparent so that we can easily perform the Kerr measurement through the thick ZnO cover layer. Besides, the ZnO/CoPd interface is stable at room temperature; capping the CoPd film by ZnO does not cause considerable change in magnetic property (Supplementary Fig. 1). The atomic structure of ZnO is quite compact so that the H_2 molecules cannot penetrate through it. Thus the ZnO cover layer can prohibit the direct contact and absorption of hydrogen from the covered surface of the CoPd

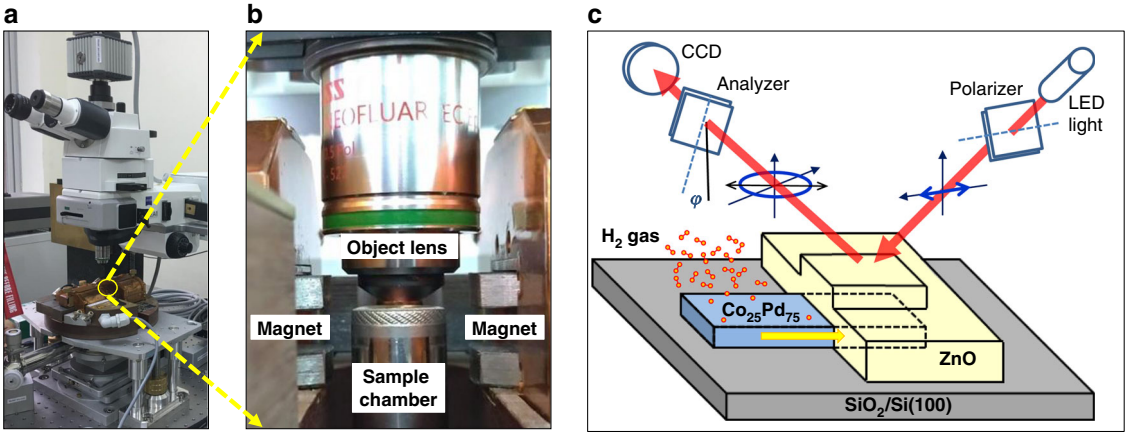

Fig. 1 Geometry of magneto-optical Kerr measurement and sample design. **a**, **b** show the photo and magnified geometry of the magneto-optical Kerr microscope with an in-plane magnetic field (i.e. the longitudinal geometry). **c** Illustration of the 50-nm-thick $Co_{25}Pd_{75}$ thin film stripe covered with 100-nm-thick ZnO. The left side of the $Co_{25}Pd_{75}$ stripe was bared for hydrogen absorption. The arrow indicates hydrogen diffusion from the bared $Co_{25}Pd_{75}$ to $ZnO/Co_{25}Pd_{75}$, as real-time monitored through magneto-optical Kerr effect

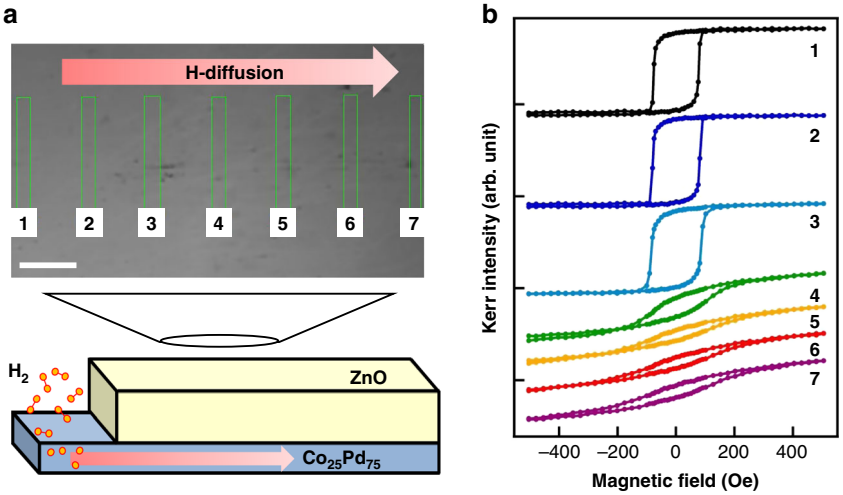

Fig. 2 Observation of hydrogen absorption-induced changes in magnetic properties. **a** Optical microscopic image of ZnO/$Co_{25}Pd_{75}$ with the bare end on the left side. The arrow indicates the hydrogen diffusion direction. The scale bar indicates 20 μm. **b** Magneto-optical Kerr effect hysteresis loops measured at various areas indicated by the rectangles in **a**. The spatially dependent evolution of magnetic hysteresis behavior indicated the hydrogen content distribution in the $Co_{25}Pd_{75}$ film

film. As illustrated in Fig. 1c, the right side of the CoPd film was fully covered by the 100-nm-thick ZnO cover layer and the left side was bare. In this sample design, we can be sure about that during the exposure to H_2 gas, the hydrogen absorption only occurs on the bare CoPd surface, and therefore the H-content in the CoPd film diffuses from the bare part (left) to the ZnO-coverd part (right). Inversely, when the chamber is evacuated, the hydrogen desorption only occurs on the bare CoPd surface and therefore the H-content diffuses from the ZnO-coverd part (right) to the bare part (left). To monitor hydrogen diffusion, the Kerr microscope focused on the boundary area with a 500 × 500-μm^2 field of vision. Sequential Kerr images were recorded using a suitable magnetic field. By integrating the intensities of selected areas in the Kerr images, we could obtain local magnetic hysteresis loops for each area. Spatially resolved magnetic behavior in the $Co_{25}Pd_{75}$ film could thus be real-time monitored during hydrogen exposure or desorption. Figure 2 illustrates an example of using longitudinal MOKE to achieve a spatially resolved hydrogenation effect. An optical microscope (OM) image is shown in Fig. 2a, with seven selected areas indicated by the green rectangles. The arrow indicates the direction of hydrogen diffusion, and the sample geometry is shown at the bottom. Hysteresis loops integrated from specific areas are shown in Fig. 2b, where the evolution of the hysteresis loop shape can clearly be seen. From left (No. 1) to right (No. 7), the hysteresis loop changes from a square-like shape to a tilted narrow shape. Our studies on Pd-rich magnetic alloy thin films have shown that the hydrogenation effect can reversibly change magnetic behavior from a low remanence (M_r) to saturation (M_s) ratio to $M_r/M_s = 100\%$[18,20,21]. This is because the hydrogen content in a Pd-rich magnetic film induces a spin-polarized charge transfer between Co and Pd, thus mediating the long-range magnetic coupling, that is, the 100% M_r/M_s ratio[18]. Because of the hydrogen-induced enhancement of magnetic exchange interaction, the Curie temperature increases and the power law dependence of M_r with temperature is elevated toward the higher temperature. Thus the room temperature-measured M_r increases with the introduction of H. Accordingly, the M_r/M_s ratio in a magnetic hysteresis loop provides a strong indicator of hydrogen content in the Pd-rich magnetic alloy film. The results shown in Fig. 2b reveal that the hydrogen diffusion front should be positioned between No. 4 and No. 5. The OM image in Fig. 2a exhibits no observable contrast around the hydrogen diffusion front. Although the Kerr rotation signal is much weaker than the background in the OM image, the Kerr effect is highly sensitive to hydrogen content and can serve as an indicator.

The $Co_{25}Pd_{75}$ alloy film under a vacuum presented no observable domain structure; the gray scale in the Kerr images gradually and continuously became darker/brighter with the negative/positive increase in the magnetic field. The absence of the magnetic domain structure is because the magnetization reversal was dominated by small nucleations which are randomly distributed on the thin film, and their size was of a submicrometer scale below the resolution of the Kerr microscope[27]. In contrast to the absence of magnetic domain structure under a vacuum, the H-content induced visible magnetic reversal nucleations and also advanced the DW motion, leading to the expansion of reversal nucleations and subsequently the large magnetic domains[27]. Besides, the magneto-optical Kerr signal (rotation) could easily change with the film thickness and protective covering layer, because the absolute value of Kerr hysteresis loop is a complex of magnetic and optical properties. The Kerr intensity I_{Kerr} is usually approximated as being proportional to the magnetization M, i.e. $I_{Kerr} \propto M$. The linear coefficient in $I_{Kerr} \propto M$ depends on the optical properties of the cover layer, magnetic thin film and the substrate. However through dividing M_r by M_s, this linear coefficient can be eliminated. The M_r/M_s ratio deduced from the Kerr hysteresis loop originates from only the intrinsic magnetism of the CoPd film. M_r/M_s is mostly determined by the exchange coupling and magnetic anisotropy, which are microscopic-scale properties. Thus in this study, we measure the spatial distribution of the M_r/M_s ratio for the indication of H-concentration. This indication by H-enhanced M_r/M_s is directly correlated to the intrinsic magnetism of CoPd film and will not be affected by the covering layer or underneath substrate. This is also the advantage of adopting the M_r/M_s ratio, especially for those non-transparent films with a covering layer.

Calibration of hydrogen concentration. In a pressure-composition-isotherms (PCI) study by Zlotea et al.[29], under an H_2 pressure of 10^5 Pa the hydrogen solubility of $Co_{25}Pd_{75}$ nanoalloys increased with decreasing particle sizes, yielding

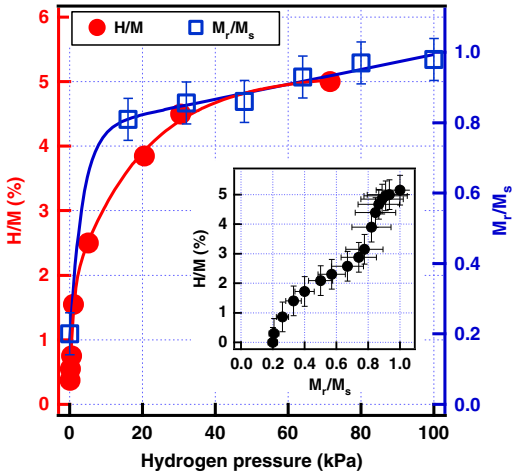

Fig. 3 Correlation between the hydrogen concentration and the remanence to saturation ratio (M_r/M_s). Left axis: atomic hydrogen (H) to metal (M) ratio; right axis: M_r/M_s ratio of $Co_{25}Pd_{75}$ when exposed to various hydrogen gas pressures[29]. The error bars are determined by the signal to noise ratio in the Kerr hysteresis loops. The inset shows the H/M ratio plotted as a function of M_r/M_s for a $Co_{25}Pd_{75}$ alloy film. This function was used in calibration of the hydrogen concentration (H/M) by measuring magneto-optical Kerr effect hysteresis loops (M_r/M_s ratio). The error bars originates from the uncertainty in the Kerr measurement

atomic hydrogen to metal ratios (H/M) of 5, 8, and 23% for average particle sizes of 12.5, 5.3, and 2.1 nm, respectively. In the case of pure Pd particles, nanosize effects are clear for particle sizes <10 nm. Therefore, it is reasonable to compare the hydrogen storage capacity of $Co_{25}Pd_{75}$ nanoalloys >10 nm to the 50-nm-thick $Co_{25}Pd_{75}$ film in our experiment. The left axis of Fig. 3 shows the PCI results of Zlotea et al.[29] for a 12.5-nm $Co_{25}Pd_{75}$ nanoalloy. The red dots depict the monotonic increasing curve of hydrogen concentration with H_2 gas pressure $\left(P_{H_2}\right)$; the H/M ratio has reached nearly 5% with 10^5 Pa of P_{H_2}. On the right axis of Fig. 3, the M_r/M_s ratio of the $Co_{25}Pd_{75}$ film is plotted as a function of P_{H_2} according to our study of the hydrogenation effect on CoPd alloys. The blue squares depict the increasing trend of the M_r/M_s ratio from 20 to 100% with the increase of P_{H_2} from 10^{-1} Pa to 10^5 Pa. By fitting the curves from the $H/M - P_{H_2}$ and $M_r/M_s - P_{H_2}$ experimental data, a correlation between hydrogen concentration (H/M) and magnetic property (M_r/M_s) was deduced, as shown in the inset of Fig. 3. According to the correlation curve, the spatial distribution of hydrogen content could be obtained from the experimentally measured M_r/M_s values. Note that all the experimental data of $H/M - P_{H_2}$ and $M_r/M_s - P_{H_2}$ were measured at room temperature (RT) and the error bars in Fig. 3 are determined from the statistical deviation of the magnetic coercivity in the repeating MOKE measurements. Considering the M_r/M_s ratio and the equilibrium H/M are sensitive to the temperature, the deduced correlation between M_r/M_s and H/M is only suitable for RT-environment.

Visualizing hydrogen diffusion. After subtracting the negative from the positive remanence state (i.e., the differential image of $(M_{r+} - M_{r-})$), the Kerr images shown in Fig. 4a clearly exhibit a time-dependent evolution of the hydrogenation effect and hydrogen content (Supplementary Fig. 2). For example, in the Kerr image for time = 600 s after H_2 exposure, the bright area on the left indicates a 100% M_r/M_s ratio because of saturated hydrogenation, whereas the dark area on the right indicates a low

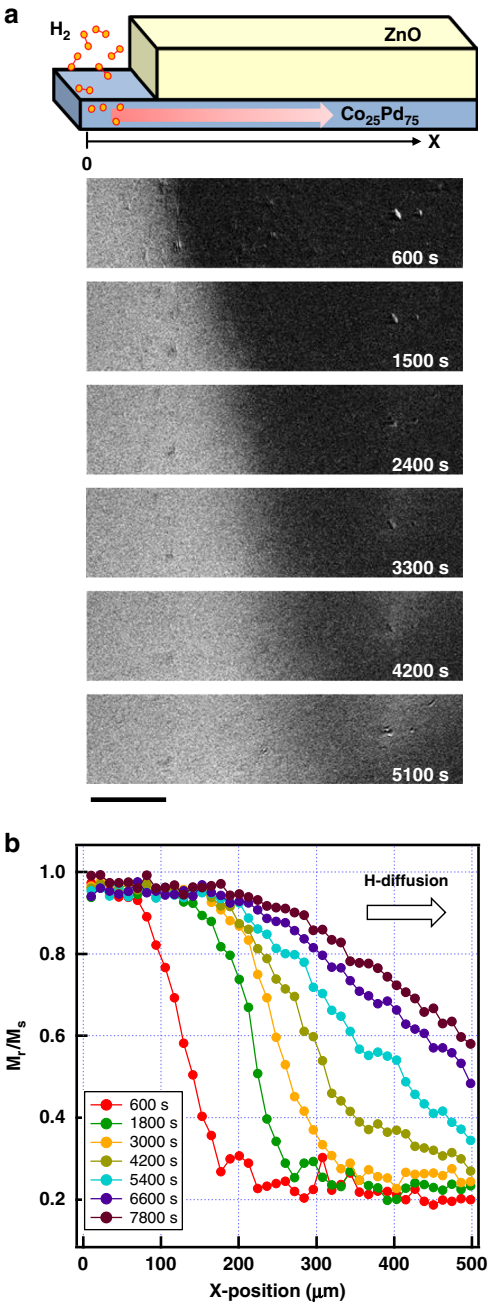

Fig. 4 Visualizing hydrogen diffusion in a 50-nm-thick $Co_{25}Pd_{75}$ film by magneto-optical Kerr effect. **a** By subtracting the negative (M_{r-}) from the positive (M_{r+}) remanence state (i.e., the differential image of $(M_{r+} - M_{r-})$), Kerr images were sequentially taken at different times after hydrogen exposure. The scale bar indicates 100 μm. **b** The the remanence to saturation ratio M_r/M_s recorded at various X positions relative to the ZnO capping layer edge. The curves correspond to different times after hydrogen exposure

M_r/M_s ratio (~20%) in the pristine $Co_{25}Pd_{75}$. In the Kerr images between 600 and 2400 s, the black/white boundary is observed to shift toward the right. After 2400 s, no obvious shift of the black/white boundary was evident; instead, the dark area gradually became gray and the contrast decreased over time. Figure 4b shows the M_r/M_s ratio recorded at various X positions relative to the edge of the ZnO capping layer. The M_r/M_s distribution was sequentially recorded at different times after hydrogen exposure. The M_r/M_s distribution curves provided information on the

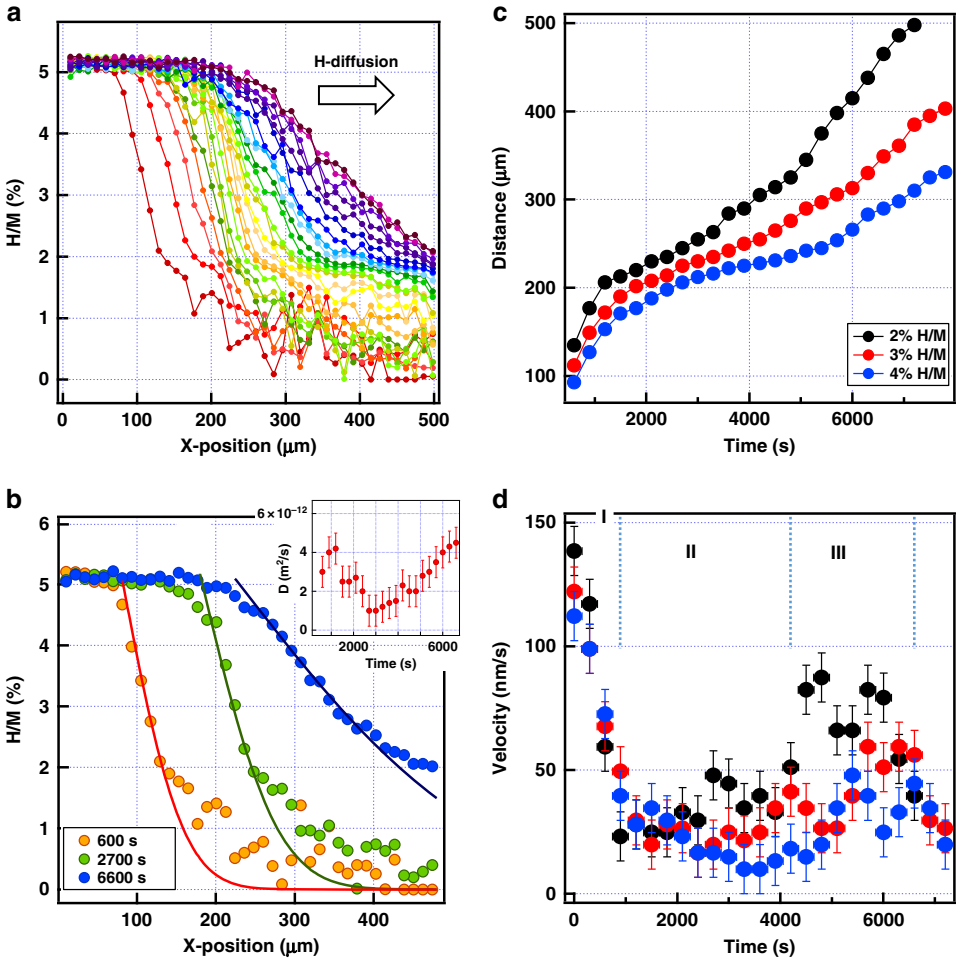

Fig. 5 Analysis of hydrogen diffusion in a 50-nm-thick $Co_{25}Pd_{75}$ film. **a** Hydrogen concentration distribution profile at different times by a step of 300 s after exposure to 10^5 Pa H_2 gas. **b** The experimental data points with the solid fitting curves. The inset shows the fitted diffusion coefficient *D* at different times with the error bars indicating the uncertainty in the fitting. **c** The position of the 2, 3, and 4% *H*/*M* fronts, plotted as a function of exposure time. **d** Velocity of the 2–4% *H*/*M* fronts derived from **c** The error bars show the statistical uncertainty in the calculation of velocity

hydrogenation effect on $Co_{25}Pd_{75}$ film magnetism. The hydrogen concentration distribution could be obtained through the correlation curve shown in Fig. 3.

The hydrogen concentration (H/M) distribution curves deduced from the M_r/M_s ratio are displayed in Fig. 5a. The position of the $H/M = 2$, 3, and 4% hydrogen diffusion fronts is plotted as a function of time in Fig. 5c. Figure 5d shows the diffusion velocity of the $H/M = 2$, 3, and 4% fronts by differentiation from the positions in Fig. 5c. Combining the information from Figs. 4b and 5, hydrogen diffusion behavior can be classified into three regions. In the first region at 0–150 μm (0–2400 s), both the Kerr image (Fig. 4b) and the *H*/*M* distribution curves (Fig. 5a) exhibit a clear hydrogen diffusion front movement. The diffusion velocity deduced from differentiation of the $H/M = 2$, 3, and 4% front positions in Fig. 5c is ~120 ± 20 nm/s. The deviation of the diffusion speed originates from the errors or uncertainties in the determination of hydrogen concentration *H*/*M*. According to the M_r/M_s-*H*/*M* correlation curve shown in Fig. 3, the spatial distribution of hydrogen content can be obtained from the experimentally measured M_r/M_s values at each location. About the spatial-resolved distribution of H-content in the $Co_{25}Pd_{75}$ film studied in this experiment, we need to consider both the spatial resolution and the resolution of H-concentration measurement. The spatial resolution is determined by the precision of our Kerr microscope, including the optical setup and the CCD-imaging system. In our experiment, the measurement results always repeated within few μm. Concerning the resolution of the H-concentration, the precision is determined by the signal to noise ratio of Kerr effect. The precision of M_r/M_s ratio is within ±0.05, corresponding to the precision of *H*/*M* ratio within ±2.5%. However the accuracy of hydrogen concentration is significantly affected by the calibration of the H-content and the M_r/M_s ratio. This calibration also counts on the previous results of Zlotea et al.[29]: the H-content in CoPd alloy corresponding to the variable hydrogen pressure. Thus the accuracy in the calibration of H-content and the M_r/M_s ratio is supposed to dominate the resolution of the H-concentration. When combining the spatial-resolved H-distribution for the fitting of diffusion coefficient, as shown in Fig. 5, the accuracy of the calibration: H-content vs. the M_r/M_s ratio determines the uncertainty.

In the second region at 150–350 μm (2400–4200 s), no clear shift of contrast in the Kerr image (Fig. 4b) or *H*/*M* distribution curves (Fig. 5a) is observed. The hydrogen concentration increased gradually. The diffusion velocity deduced from differentiation of the $H/M = 2$, 3, and 4% front positions in Fig. 5c is ~30 ± 15 nm/s. In this region, hydrogen diffusion is relatively low and follows Fick's diffusion laws[8]. Considering the low concentration of *H*/*M* (≤5%) and the fact that measurement was performed at 300 K, hydrogen behaved as a noninteracting particle and accordingly followed Fick's second diffusion law,

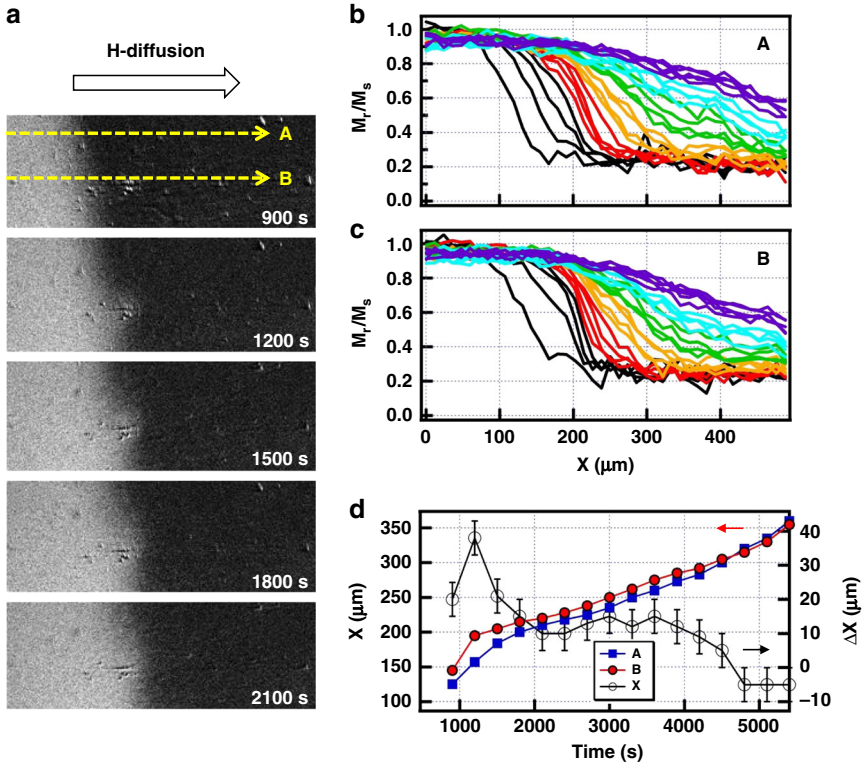

Fig. 6 Hydrogen diffusion across a defect site. **a** By subtracting the negative from the positive remanence state (i.e., the differential image of ($M_{r+} - M_{r-}$)), Kerr images were sequentially taken at different times when hydrogen diffused across a defect area. **b**, **c** Remanence to saturation ratio M_r/M_s recorded at various X positions along lines A and B, as indicated in **a**. The curves correspond to different times after the start of hydrogen absorption from the bared $Co_{25}Pd_{75}$. **d** Left axis: position of the 2% *H*/*M* (*H*/*M*: atomic hydrogen (*H*) to metal (*M*) ratio) front in normal area (line A) and across the defect (line B) plotted as a function of time; right axis: difference between the 2% *H*/*M* front position on lines A and B. The error bars are determined by the uncertainty in 2% *H*/*M* front positions

which can be expressed as follows:

$$\frac{\partial C(x,t)}{\partial t} = D\frac{\partial^2 C(x,t)}{\partial^2 x} \quad (1)$$

where C(*x*, *t*) is the time (*t*)- and position (*x*)-dependent function of the hydrogen concentration *H*/*M*, and *D* is the diffusion coefficient, which can be determined by fitting the model to the data[8]. Actually we followed the simulation method as reported by Pálsson et al.[8]. Given the boundary and initial conditions for the sample geometry in this experiment, the solution of Eq. (1) is expressed as a series of complementary error functions (erfcs)[8]. The erfc series converges quickly, and only a few terms must be considered when fitting the data[8]. The *H*/*M* distribution curves in the second region were fitted by solving Eq. (1) with a single free parameter, namely the diffusion coefficient *D*[8]. By fitting the experimental data with the model, a diffusion coefficient *D* was obtained. Figure 5b shows examples of the fitting curves and the inset summarizes the fitted values of *D* at the various times. From the fitted *D* values, we obtained an average $D = 3 \pm 2 \times 10^{-12}$ m^2/s. In other studies of Y, V, and Y/V bilayer thin films, *D* varies at room temperature by four orders of magnitude between the extreme values of H in Y (typically 10^{-13} m^2/s) and H in V (typically 10^{-9} m^2/s)[7]. For Mg-dihydride thin films, Teichmann et al. reported an average effective hydrogen diffusion coefficient of $\sim 3 \times 10^{-12}$ m^2/s at room temperature[30]. The D value of $3 \pm 2 \times 10^{-12}$ m^2/s for hydrogen diffusion in $Co_{25}Pd_{75}$ alloy thin film is within the *D* range observed in other studies and close to the *D* values in YH_x and MgH_x systems. Based on this MOKE method, detection of *D* values can be performed in other magnetic transition-metal hydrides.

In the third region at 350–500 μm (4200–6500 s), the diffusion velocity deduced from differentiation of the *H*/*M* = 2, 3, and 4% front positions in Fig. 5c is ~50 ± 20 nm/s, which is much faster than in the second region. When examining the optical image, a defect site on the hydrogen diffusion passage was found to dominate enhancement of the hydrogen diffusion velocity. To confirm the mechanism, more detailed analysis of the difference between the hydrogen diffusion velocity in a uniform area and that across a defect site was performed. Figure 6a shows the contrasted Kerr image ($M_{r+} - M_{r-}$) near a defect site for different hydrogen diffusion times. When the hydrogen front approached the defect site at ~1200 s, a protruding domain was produced across the defect. In Fig. 6b, c, the spatial distribution of the M_r/M_s ratio is illustrated sequentially for different times on line profiles A and B, which pass through a normal film area and a defect area, respectively, as indicated in Fig. 6a. In the left axis of Fig. 6d, the position of the 2% *H*/*M* front diffusing along line A (beside the defect) and line B (across the defect) is plotted as a function of time. In the right axis, the difference between the 2% *H*/*M* front position along lines A and B (ΔX) is plotted, indicating the relatively rapid hydrogen diffusion rate across the defect area at ~1200 s. After passing through the defect area, diffusion of the 2% hydrogen front along lines A and B gradually merged at ~4800 s. This remerging of the hydrogen diffusion front after passing through the defect area seems reasonable, because transverse hydrogen diffusion could gradually eliminate the hydrogen concentration gradient between lines A and B.

Along with hydrogen absorption and diffusion, hydrogen desorption from the $Co_{25}Pd_{75}$ alloy film was also real-time monitored, as shown in Fig. 7. After loading the hydrogen

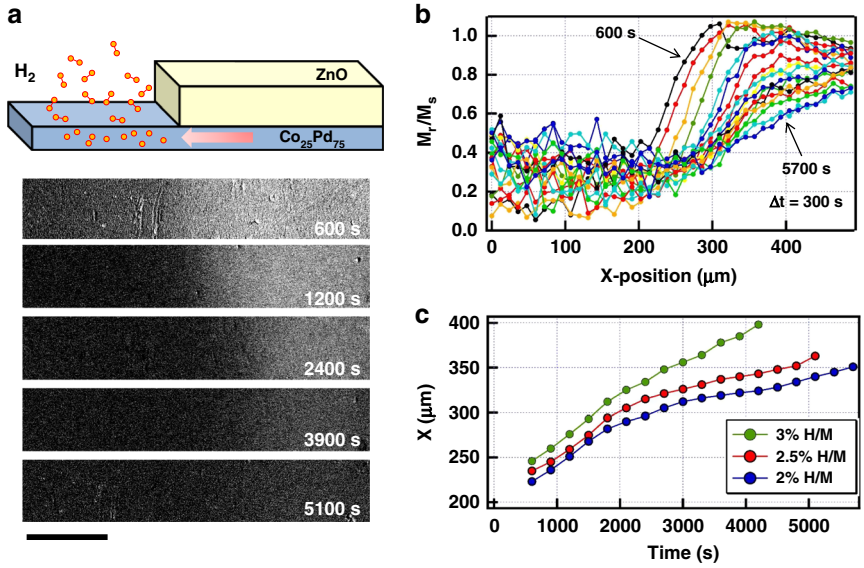

Fig. 7 Analysis of hydrogen movement during desorption. **a** By subtracting the negative from the positive remanence state (i.e., the differential image of ($M_{r+} - M_{r-}$)), Kerr images were sequentially taken at different times after hydrogen desorption started. The scale bar indicates 100 μm. **b** Remanence to saturation ratio M_r/M_s recorded at various X positions. The curves correspond to different times after the start of hydrogen desorption from the bared $Co_{25}Pd_{75}$. **c** Time-dependent position of 2, 2.5, and 3% *H*/*M* (*H*/*M*: atomic hydrogen (*H*) to metal (*M*) ratio) fronts across the defect-free area

concentration to nearly 5% of *H*/*M* by exposure to 10^5 Pa hydrogen gas, the hydrogen gas was pumped out to create a vacuum of 5×10^{-1} Pa for investigation of hydrogen desorption. Because the bared area of $Co_{25}Pd_{75}$ was exposed to a vacuum, the hydrogen desorption rate became much higher than the adsorption rate at the bared surface, leading to net hydrogen desorption. A one-dimensional hydrogen concentration gradient thus formed, leading to unidirectional hydrogen diffusion from the ZnO-covered region to the bared $Co_{25}Pd_{75}$ region. As illustrated in Fig. 7a, at the start of hydrogen desorption (600 s) the bared $Co_{25}Pd_{75}$ area (left) became dark (i.e., low M_r/M_s ratio and hydrogen concentration), whereas the ZnO-covered area (right) remained bright (i.e., high M_r/M_s ratio and hydrogen concentration). With increasing desorption time, the dark/bright boundary moved rightward to the ZnO/$Co_{25}Pd_{75}$ area, which also gradually became darker. Figure 7b shows the time-dependent M_r/M_s curves plotted as a function of position X, and Fig. 7c the time-dependent position of the 2, 2.5, and 3% *H*/*M* fronts across the defect-free area. The quantitative results of hydrogen desorption (Fig. 7b, c) are similar to the hydrogen absorption behavior in Fig. 5a, b. During the first 1000 s, the diffusion rate reached approximately 50 ± 20 nm/s, followed by a relatively low speed of ~30 ± 15 nm/s. The similarity of hydrogen absorption and desorption behaviors indicates that the same diffusion mechanism—namely, Fick's diffusion law—prevailed.

The main idea of this report is that H-content promoted magnetic exchange interaction and caused the increase of M_r. This is because the H-content enhanced the magnetic exchange interaction. In our Kerr measurement, the sample of ZnO-covered $Co_{25}Pd_{75}$ alloy thin film was stored in a chamber at RT while the hydrogen pressure in the chamber was stably sustained at 1 bar. The experimental results demonstrated that the material of $Co_{25}Pd_{75}$ alloy and the method of spatial-resolved magneto-optical Kerr effect could be used for the hydrogen gas sensing and the indicator of H-content distribution in solids at the constant temperature of RT. However one should note that when the hydrogen content in a material reaches an equilibrium condition, an equal amount of hydrogen is entering and leaving the sample. This equilibrium counts on the equality between the absorption and desorption rate of hydrogen. If some external conditions change, such as the temperature or hydrogen pressure, the absorption rate and desorption rate may considerably be changed and thus a new equilibrium state with different hydrogen concentration will be achieved. Therefore our method cannot be directly applied at variable temperature or under a P_{H_2} other than 1 bar, unless the H-induced change in M_r is calibrated in the various conditions.

Discussion

In this study, hydrogen diffusion in an $Co_{25}Pd_{75}$ alloy film was real-time monitored using a magneto-optical Kerr microscope. Through hydrogenation-induced enhancement of magnetic remanence, the *H*/*M* atomic ratio could be calibrated using spatially resolved magneto-optical contrasted images. This method provided a noninvasive method of monitoring hydrogen movement in magnetic thin film. In our analysis, hydrogen absorption and diffusion followed Fick's diffusion law, and a diffusion coefficient of $3 \pm 2 \times 10^{-12}$ m^2/s was obtained by fitting the experimental data to the model. The diffusion velocity of the 2, 3, and 4% hydrogen concentration fronts reached 30 ± 15 nm/s in the uniform film area and increased to 50 ± 20 nm/s near a defect site. Hydrogen desorption exhibited a hydrogen diffusion speed similar to that of hydrogen absorption. These results demonstrated that hydrogen diffusion in nontransparent Pd-rich magnetic alloy thin films could be monitored, with possible applications in hydrogen-sensing and -storage technology.

Along with monitoring hydrogen diffusion behavior in magnetic metal thin films, we also demonstrated that the hydrogen-induced magnetic boundary was within 100 μm, which is even smaller than the general size of in-plane magnetic domains. This indicated that the hydrogen concentration gradient in magnetic CoPd film could induce a critical difference in interatomic magnetic coupling and lead to a discontinuity in magnetic domain structure. Even in a continuous $Co_{25}Pd_{75}$ alloy film, the expected large-scale long-range magnetic coupling did not mantle the hydrogen-induced contrast in Kerr images. The drastic hydrogen-induced change in local magnetic behavior, namely the enhanced M_r/M_s ratio, was sufficiently strong to overcome the pristine magnetic coupling. These observations suggest the future applicability of magnetic patterning using hydrogen implantation or diffusion.

Methods

Sample preparation. The ZnO/$Co_{25}Pd_{75}$ sample structure was fabricated on a SiO_2/Si(001) substrate, as shown in Fig. 1. A 50-nm-thick $Co_{25}Pd_{75}$ alloy thin film, masked in the form of a 1×3-mm^2 stripe, was codeposited by e-beam-heated evaporators in an ultra-high vacuum chamber with a base pressure of 3×10^{-7} Pa. The film thickness and alloy composition were calibrated through Auger electron spectroscopy, transmission electron microscopy coupled with energy dispersive spectroscopy, and atomic force microscopy[18,20]. A 100-nm-thick ZnO film was subsequently deposited on part of the $Co_{25}Pd_{75}$ film, leaving one end of $Co_{25}Pd_{75}$ stripe bared. The ZnO film was prepared at room temperature in an oxygen ambient pressure of 8.0 Pa through pulsed-laser deposition[31]. A Nd:YAG Q-switch laser provided a laser wavelength of 266 nm with an energy density of approximately 2.7 J/cm^2[31,32].

Magnetic measurement. The magnetic hysteresis loops of the $Co_{25}Pd_{75}$ film were measured at room temperature using a magneto-optical Kerr microscope (Evico Magnetics GmbH) in the longitudinal geometry, focused on the boundary area between ZnO/$Co_{25}Pd_{75}$ and bared $Co_{25}Pd_{75}$. Magneto-optical Kerr effect (MOKE) measurements were conducted in a small vacuum chamber equipped with a window[27]. During measurement, the MOKE chamber was either pumped to a vacuum of 5×10^{-1} Pa or filled with H_2 gas at various pressures to investigate the hydrogen effect on the magnetic properties of the $Co_{25}Pd_{75}$ alloy films.

Data availability

The authors declare that the raw data supporting the findings of this study (Figs. 2–7) are available from the corresponding author on reasonable request.

Received: 18 October 2018 Accepted: 21 June 2019
Published online: 30 July 2019

References

1. Delmelle, R. & Proost, J. An in situ study of the hydriding kinetics of Pd thin films. *Phys. Chem. Chem. Phys.* **13**, 11412 (2011).
2. Bartczak, W. M. & Stawowska, J. Interaction of dihydrogen with transition metal (Pd, Ni, Ag, Cu) clusters. *Struct. Chem.* **15**, 447 (2004).
3. Huiberts, J. N. et al. Yttrium and lanthanum hydride films with switchable optical properties. *Nature* **380**, 231–234 (1996).
4. Lederman, D. et al. Magnetooptic properties of Fe/Pd andCo/Pd bilayers under hydrogen absorption. *Appl. Phys. Lett.* **85**, 615 (2004).
5. den Broeder, F. J. A. et al. Visualization of hydrogen migration in solids using switchable mirrors. *Nature* **394**, 656–658 (1998).
6. Kerssemakers, J. W. J., van der Molen, S. J., Koeman, N. J., Günther, R. & Griessen, R. Pixel switching of epitaxialPd/Y H_x/CaF_2 switchable mirrors. *Nature* **406**, 489–491 (2000).
7. Remhof, A. et al. Switchable mirrors for visualization and control of hydrogen diffusion in transition metals. *Phys. Rev. B* **66**, 020101(R) (2002).
8. Pálsson, G. K., Bliersbach, A., Wolff, M., Zamani, A. & Hjörvarsson, B. Using light transmission to watch hydrogen diffuse. *Nat. Commun.* **3**, 892 (2012).
9. Klose, F., Rehm, C., Nagengast, D., Maletta, H. & Weidinger, A. Continuous and reversible change of the magnetic coupling in an Fe/Nb multilayer induced by hydrogen charging. *Phys. Rev. Lett.* **78**, 1150 (1997).
10. Hjörvarsson, B. et al. Reversible tuning of the magnetic exchange coupling in Fe/V(001) superlattices using hydrogen. *Phys. Rev. Lett.* **79**, 901 (1997).
11. Zhang, W., Luo, S. & Flanagan, T. B. Hydrogen solution in homogeneousPd–Fe alloys. *J. Alloy. Compd* **1–6**, 293–295 (1999).
12. Wang, D., Lee, K.-Y., Luo, S. & Flanagan, T. B. The thermodynamics of hydrogen absorption/desorption by Pd–Co alloys. *J. Alloy. Compd* **252**, 209–218 (1997).
13. Lueng, C., Lupo, P., Metaxas, P. J., Kostylev, M. & Adeyeye, A. O. Nanopatterning-enhanced sensitivity and response time of dynamic Palladium/Cobalt/Palladium hydrogen gas sensors. *Adv. Mater. Technol.* **1**, 1600097 (2016).
14. Lin, W. C., Tsai, C. J., Wang, B. Y., Kao, C. H. & Pong, W. F. Hydrogenation induced reversible modulation of perpendicular magnetic coercivity in Pd/Co/Pd films. *Appl. Phys. Lett.* **102**, 252404 (2013).
15. Munbodh, K. et al. Effects of hydrogen/deuterium absorption on the magnetic properties of Co/Pd multilayers. *Phys. Rev. B* **83**, 094432 (2011).
16. Lin, W. C., Tsai, C. J., Liu, X. M. & Adeyeye, A. O. Critical hydrogenation effect on magnetic coercivity of perpendicularly magnetized Co/Pd multilayer nanostructures. *J. Appl. Phys.* **116**, 073904 (2014).
17. Munbodh, K., Perez, F. A. & Lederman, D. Changes in magnetic properties of Co/Pd multilayers induced by hydrogen absorption. *J. Appl. Phys.* **111**, 123919 (2012).
18. Lin, W. C. et al. Hydrogen-mediated long-range magnetic ordering inPd-rich alloy film. *Appl. Phys. Lett.* **106**, 12404 (2015).
19. Gerber, A., Kopnov, G. & Karpovski, M. Hall effect spintronics for gas detection. *Appl. Phys. Lett.* **111**, 143505 (2017).
20. Lin, W. C., Wang, B. Y., Huang, H. Y., Tsai, C. J. & Mudinepalli, V. R. Hydrogen absorption-induced reversible change in magnetic properties of Co-Pd alloy films. *J. Alloy. Compd* **661**, 20–26 (2016).
21. Liang, J. Y. et al. Using magnetic structure of$Co_{40}Pd_{60}$/Cu for the sensing of hydrogen. *Appl. Phys. Lett.* **111**, 023503 (2017).
22. Chang, C. S., Kostylev, M. & Ivanov, E. Metallic spintronic thin film as a hydrogen sensor. *Appl. Phys. Lett.* **102**, 142405 (2013).
23. Chang, P. C., Chen, Y. C., Hsu, C. C., Chiu, H. C. & Lin, W. C. Hydrogenation-induced reversible spin reorientation transition in $Co_{50}Pd_{50}$ alloy thin films. *J. Alloy. Compd* **710**, 37–46 (2017).
24. Zhang, W., Liu, Z., Belotelov, V. I., Wang, Q. & Song, Y. The magnetic properties of CoFeB and CoFeB/Ag nanodot arrays fabricated by a template transfer imprinting method. *Thin Solid Films* **660**, 301–305 (2018).
25. Zhang, W. et al. Tunable magneto-optical Kerr effects of nanoporous thin films. *Sci. Rep.* **7**, 2888 (2017).
26. Bossini, D., Belotelov, V. I., Zvezdin, A. K., Kalish, A. N. & Kimel, A. V. Magnetoplasmonics and femtosecond optomagnetism at the nanoscale. *ACS Photon.* **3**, 1385–1400 (2016).
27. Chang, P.-C., Liu, C.-M., Hsu, C.-C. & Lin, W.-C. Hydrogen-mediated magnetic domain formation and domain wall motion in $Co_{30}Pd_{70}$ alloy films. *Sci. Rep.* **8**, 6656 (2018).
28. Lin, W. C. et al. Hydrogenation-induced change of magneto optical kerr effect in Pd/Fe bilayers. *J. Appl. Phys.* **112**, 63914 (2012).
29. Zlotea, C. et al. Hydrogen sorption properties of Pd–Co nanoalloys embedded into mesoporous carbons. *Nanoscale* **7**, 15469–15476 (2015).
30. Teichmann, N., Hamm, M. & Pundt, A. Fast lateral hydrogen diffusion in magnesium-hydride films on sapphire substrates studied by electrochemical hydrogenography. *Int. J. Hydrog. Energy* **43**, 1634–1642 (2018).
31. Lin, W. C., Chang, P.-C., Tsai, C.-J., Shieh, T.-C. & Lo, F.-Y. Voltage-induced reversible changes in the magnetic coercivity of Fe/ZnO heterostructures. *Appl. Phys. Lett.* **104**, 062411 (2014).
32. Lo, F. Y. et al. Paramagnetic dysprosium-doped zinc oxide thin films grown by pulsed-laser deposition. *J. Appl. Phys.* **117**, 213911 (2015).

Acknowledgements

This study was financially supported by the Ministry of Science and Technology of Taiwan under grants nos. MOST 105-2628-M-003-001-MY3 and MOST 105-2633-M-003-001.

Author contributions

W.C.L. and F.Y.L. conceived the experiments. P.C.C. and Y.Y.C. conducted the experiments. W.C.L., P.C.C., and W.H.W. analyzed the results.

Additional information

Supplementary information accompanies this paper at https://doi.org/10.1038/s42004-019-0189-1.

Competing interests: The authors declare no competing interests.

Reprints and permission information is available online at http://npg.nature.com/reprintsandpermissions/

Publisher's note: Springer Nature remains neutral with regard to jurisdictional claims in published maps and institutional affiliations.